CHINESE OPTICS LETTERS

Vol. 19, No. 12 | December 2021

Recognizing local artifacts in two-photon imaging of dendrites beneath blood vessels *in vivo*

Cheng Jin (靳 程)[1], Ruheng Shi (施汝恒)[1], Chi Liu (刘 驰)[1], and Lingjie Kong (孔令杰)[1,2*]

[1] State Key Laboratory of Precision Measurement Technology and Instruments, Department of Precision Instrument, Tsinghua University, Beijing 100084, China

[2] IDG/McGovern Institute for Brain Research, Tsinghua University, Beijing 100084, China

*Corresponding author: konglj@tsinghua.edu.cn

Received April 12, 2021 | Accepted May 21, 2021 | Posted Online September 6, 2021

Localized wavefront aberrations would introduce artifacts in biomedical imaging, which, however, are often neglected, as their compensations are at the cost of the field-of-view. Here, we show rarely reported local artifacts in two-photon imaging of dendrites beneath blood vessels in a mouse brain *in vivo* and interpret the phenomena via numerical simulations. The artifacts of divided parallel structures are found to be induced by coma and astigmatism, resulting from sample tilting and the cylinder shape of vasculatures, respectively. Different from that in single-photon microscopy, such artifacts in nonlinear microscopy show unique characteristics and should be recognized for proper interpretation of the images.

Keywords: biomedical imaging; two-photon microscopy; wavefront aberration; artifacts of dendrites; mouse cortex.
DOI: 10.3788/COL202119.121701

1. Introduction

Benefiting from minimal invasion, high resolution, high sensitivity, *etc*., optical imaging of biodynamics provides a large number of physiological and pathological information[1–4]. As a specific example, it plays a vital role in neuroscience for both structural imaging and functional imaging[5,6]. In the study of neural plasticity, by the time-lapse imaging of dendrites and spines, one can infer the re-wiring of neural circuits based on their morphology changes[7–9]. High resolution has always been a goal in optical imaging[10]. However, optical imaging in biological tissue is susceptible to wavefront aberration, which would distort the diffraction limited point-spreading function (PSF) and deteriorate the imaging resolution and contrast[11]. Even worse, the wavefront aberration may induce image artifacts, which, if not recognized, would lead to improper conclusions.

In general, a wavefront aberration is classified as system aberration and sample aberration[12]. The former one is related to non-ideal designing and processing of optical devices, the alignment error during system adjustment, and the misalignment between imaging samples and optical systems. The latter one is induced by the random refraction and scattering in tissues, as a result of the heterogeneity and non-uniformity of biological samples.

For the conventional wide-field fluorescence microscopy (WFM) based on single-photon excitation, a wavefront aberration suffered by the emission fluorescence is the main concern, which would deteriorate the optical resolution and introduce cross talk[13]. For deep-tissue imaging, two-photon microscopy (TPM) was proposed[14] and has been widely adopted in *in vivo* imaging[15]. In TPM, longer excitation wavelengths are adopted to resist tissue scattering, and the localization of signal excitation ensures that all emission photons, including ballistic and scattered photons, contribute to the signals. Compared to that in WFM, the wavefront aberration suffered by the excitation light in TPM becomes the main concern.

To compensate wavefront aberrations, several wavefront engineering techniques[16–18], including adaptive optics[19,20], have been developed and successfully applied in bioimaging. However, the effective area with wavefront compensation gets narrower as high-order wavefront aberrations show up[21]. Even though advanced techniques, such as multi-pupil adaptive optics[22], have been proposed to enlarge the effective field-of-view (FoV) by independently compensating the wavefront aberrations of sub-FoVs, they still fail in high-speed, large FoV imaging of tissues with localized and isolated aberrations (such as those arisen from blood vessels). In such scenarios, the adoption of adaptive optics becomes less valuable, and one would rather choose a conventional imaging system, where, however, possible artifacts should be noticed.

Here, we demonstrate an observation of local artifacts in two-photon imaging of dendrites beneath blood vessels in a mouse brain *in vivo*, which are shown as divided parallel structures at certain imaging depths. To interpret the experimental results, we perform 3D numerical simulations of TPM and find that the local artifacts are induced by the hybrid effect of coma and

astigmatism. We also compare the effect of these wavefront aberrations in conventional WFM and TPM and show that the artifacts in nonlinear microscopy are unique.

2. Materials and Methods

The experimental setup is similar to conventional TPMs[23]. The femtosecond laser is tuned to 920 nm, and a water immersion objective lens (NA = 0.8, $n = 1.33$) is employed, which ensures that the theoretically lateral and axial resolutions are 0.43 μm and 2.15 μm, respectively. We use Thy1 yellow fluorescent protein (YFP) (H line) transgenic mice (Jax Stock No: 003782) for *in vivo* chronic imaging after a craniotomy, in which neurons are labeled with YFP sparsely.

In numerical simulations, we adopt the vector diffraction theory to calculate the PSF[24,25], considering a high NA objective is used. Moreover, we choose an ideal plane wave with x-linear polarization and adopt Zernike modes to describe wavefront aberrations[26,27]. Since the interested FoV is very small, wavefront aberration can be considered to be approximately unchanged. Therefore, PSF distortion caused by wavefront aberration can be considered to be spatially invariant, which helps to reasonably simplify the simulation model, i.e., images at different positions can be regarded as 3D convolution of the same distorted PSF as the sample.

To verify the influence of wavefront aberration on imaging quality, we generate a 3D dendrite model. First, we define the central axial depth z_f of the dendrite and a few of feature points on the corresponding XY section to give a preliminary idea of the shape of the dendrites, as the red stars shown in Fig. 1(a). Then, the central axes (x_s, y_s) of the 3D dendrite are generated by cubic spline interpolation of these feature points, as shown in Fig. 1(a).

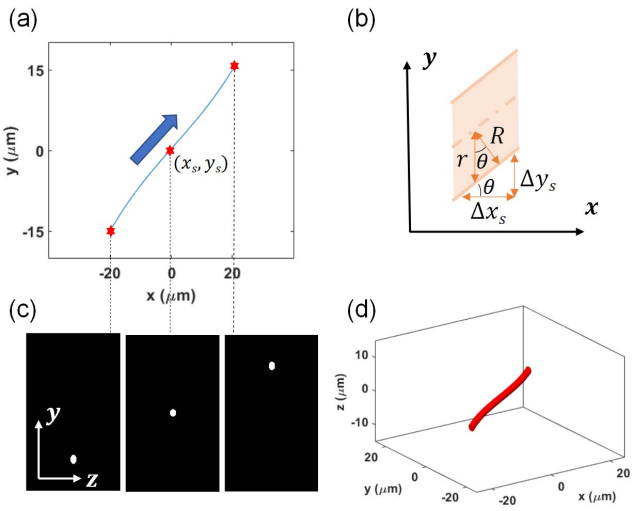

Fig. 1. Dendrite 3D simulation model. (a) Central axis of dendrites. The coordinate (x_s, y_s) of a feature point is shown. (b) Modification of dendritic radius. Here, θ is the incline angle between the orthogonal direction of the dendrites (i.e., the direction of the dendritic radius) and the y axis. (c) Typical YZ cross sections at different x_s. (d) Generated 3D dendrite model where $z_f = 0$.

Then, each YZ section of the 3D dendrite is calculated. The radius of the dendrite is defined as R. Since there is an incline angle between dendrites and y axis, the radius r of the cross section in the y direction needs to be modified according to the angle, as shown in Fig. 1(b).

The modified radius r satisfies

$$r = R/\cos[\arctan(\Delta y_s/\Delta x_s)]. \tag{1}$$

We traverse the entire dendrite by changing x_s along the blue arrow in Fig. 1(a). The projection of a 3D dendrite with a radius R on the YZ cross section is an ellipse centered at (y_s, z_f) with a major axis of r and a minor axis of R, so, at each YZ cross section, the point that meets

$$[(y - y_s)/r]^2 + [(z - z_f)/R]^2 \le 1 \tag{2}$$

will be deemed as a part of the dendrite.

3. Results

3.1. Experimental observation of local artifacts in two-photon imaging of mouse cortex *in vivo*

In practical imaging, wavefront aberrations caused by both optical systems and biological samples would deteriorate the image quality or, even worse, induce artifacts. We show a two-photon imaging stack of YFP labeled neurons recorded in the mouse cortex *in vivo* [Fig. 2(a)]. It can be seen that there is a large blood vessel at the superficial cortex in the FoV, which can be inferred from the dark region of the maximum intensity projection in the XY plane [Fig. 2(b), upper], as the absorption coefficients of oxyhemoglobin and deoxyhemoglobin are higher than that of water in the visible and near infrared regions[28]. Beneath the large blood vessel, there are some dendrites shown as single lines at certain imaging depths, but shown as closely spaced double lines at neighboring depths [Figs. 2(d)–2(f)], which are at the depth of ∼30 μm. We show the intensities along solid lines in Fig. 2(g), which indicates that the peak intensity of each dendrite is divided into two with the shifting of the imaging depth. Meanwhile, the dendrite position has a lateral shift with the increase of imaging depth, which could be indicated from the maximum intensity pixel position in Fig. 2(g). We also notice that the artifacts only show up for the dendrites oriented along the big blood vessel. However, for the dendrites whose orientations are perpendicular to the big blood vessel above, no such artifact is observed. We show the intensity along dotted lines in Figs. 2(d)–2(f) to verify this observation [Fig. 2(h)]. It should also be noted that no such artifacts are observed for regions beyond the shadow of the large blood vessel, which suggests that the contribution of the blood vessel on the local artifacts cannot be neglected.

Moreover, we check the sample alignment for potential factors of the artifacts and find that the surface of the mouse cortex is tilted relative to the focal plane, with a tilt angle of $\theta = 2.4°$, which could also induce wavefront aberrations [Fig. 2(b), lower].

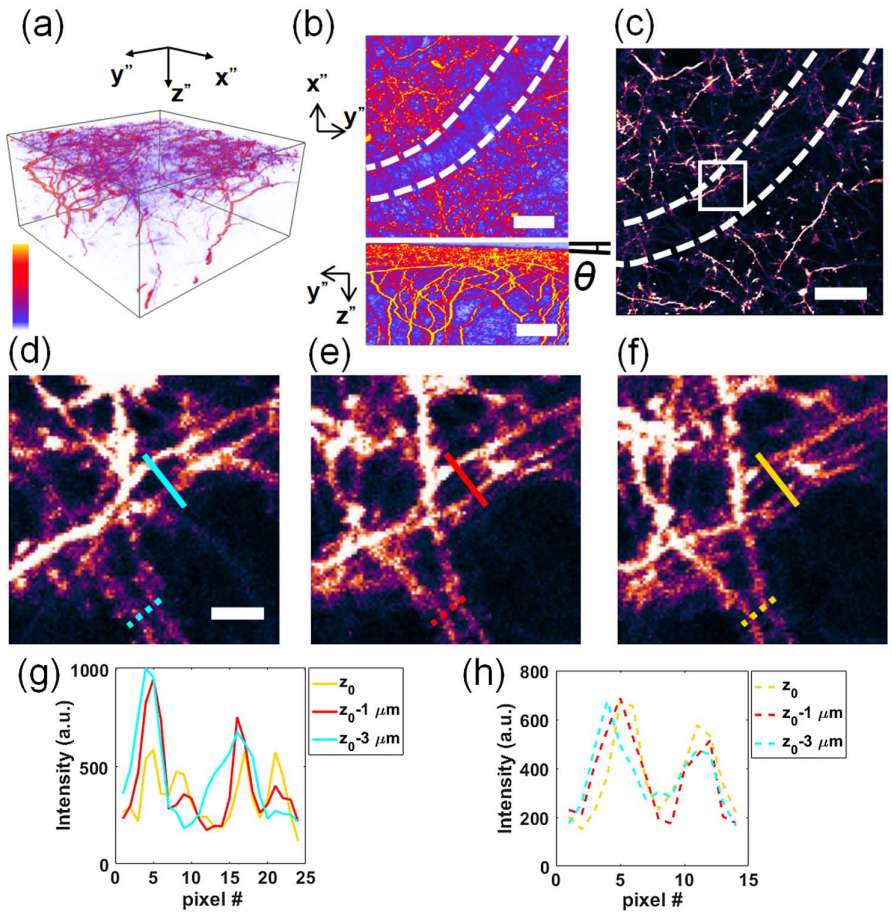

Fig. 2. Experimental results of two-photon imaging in the Thy1-YFP mouse cortex *in vivo*. (a) Imaging stack of the Thy1-YFP mouse cortex. Volume size: 520 μm × 520 μm × 420 μm. (b) Upper: the maximum intensity projection in the *XY* plane. The white dotted curve shows the boundary of the large blood vessel. Lower: the maximum intensity projection in the *YZ* plane. The auxiliary line shows the angle between the sample surface and the imaging surface. Scale bar: 100 μm. (c) A superficial plane in the imaging stack. The white dotted curve shows the boundary of the large blood vessel. Scale bar: 100 μm. (d)–(f) Typical cross sections beneath the large blood vessel of the imaging stack at different depths. Here, the z_0 plane is defined at a depth in the stack where the close double dendrites appear the most obviously. (d)–(f) show the same area in the box in (c). Scale bar: 20 μm. (g) Intensities along solid lines in (d)–(f). (h) Intensities along dotted lines in (d)–(f).

3.2. Numerical simulations to interpret the experimental artifacts

To explain the phenomena observed above, we perform numerical simulations of two-photon imaging with wavefront aberrations. As shown above, the cylindrical shape of the blood vasculature and sample tilting are two possible sources of wavefront aberration, with the former one inducing astigmatism[29,30] and latter one inducing coma[31].

In Fig. 3, we simulate the effect of these two aberrations on 3D PSF and two-photon images of the dendrite model, separately. In the dendrite model, there are three dendrites, in which two are at $z_f = 0$, and the third is at $z_f = 5\,\mu\text{m}$ [Fig. 3(a)].

We show the 3D PSF under the effect of the fundamental-order astigmatism, which has two foci that are symmetric about the z axis and orthogonal in the XY plane [Fig. 3(b)]. In numerical simulation results of the dendrite model in TPM imaging, the astigmatic PSF causes double-dendritic artifacts along the axial direction, while it has different effects on dendrites in orthogonal directions in lateral planes [Fig. 3(d)]. Because each focus contains two main energy lobes, when one lobe of the focus and a dendrite are parallel, the image intensity is higher. The astigmatic PSF results in a double-dendritic phenomenon in the lateral direction at the z_0 plane, but the intensity at the z_0−3 μm plane is very weak, which cannot interpret the experiment results well [Fig. 3(l)]. In addition, we show the 3D PSF under the effect of the fundamental-order coma [Fig. 3(c)], which has transverse tailing and lateral shifts compared with the transform limited PSF. In the TPM imaging simulation of the dendrites model, the axial resolution of dendritic images becomes worse because of coma [Fig. 3(e)]. Coma also causes the maximum intensity position to shift laterally at different depths [Fig. 3(m)], which is one of the phenomena observed in the experiment. But, coma alone does not introduce double dendrites artifacts.

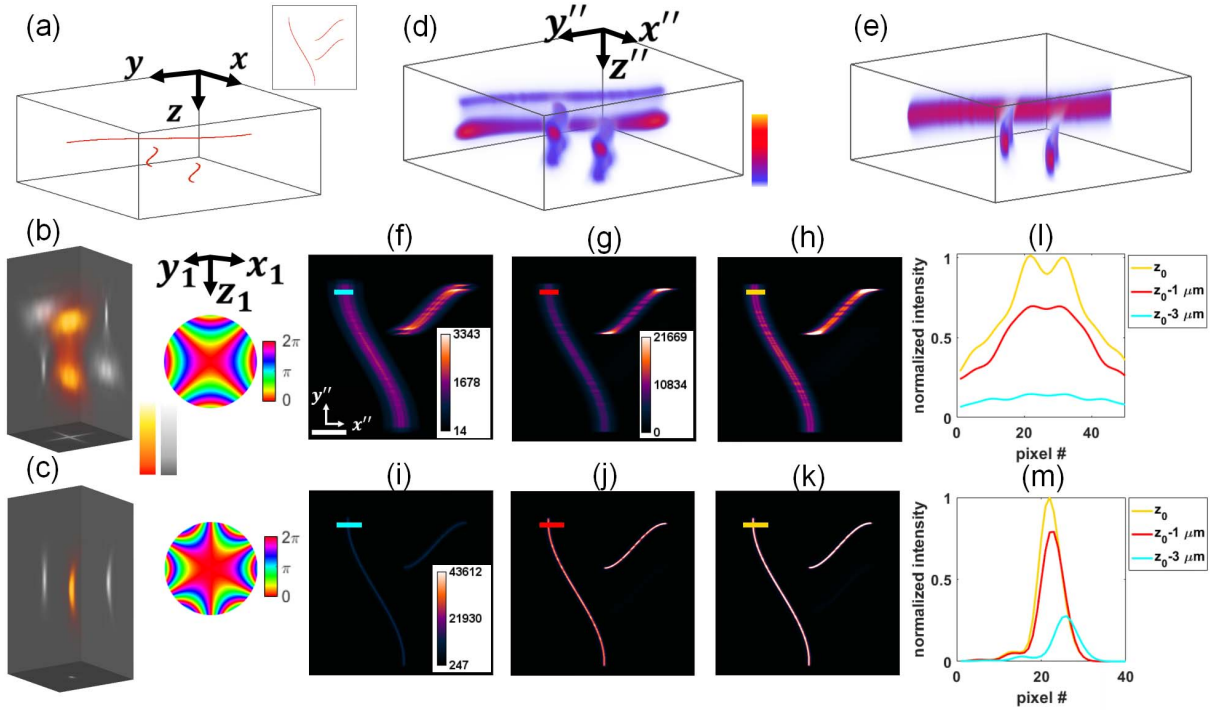

Fig. 3. Numerical simulation of distorted 3D PSFs and the TPM images of the dendrite model under the astigmatism and coma, separately. (a) 3D distribution of the dendrite model with a diameter of 0.2 μm. Inset: the maximum intensity projections in the *XY* plane. Volume size: 50 μm × 50 μm × 20 μm. (b) Distorted 3D PSF under the effect of the fundamental-order astigmatism Z_2^2, with Zernike coefficient W_2^2 = 0.3 μm. (c) Distorted 3D PSF under the effect of the fundamental-order coma Z_3^1, with Zernike coefficient W_3^1 = 0.1 μm. In (b) and (c), both the 3D normalized intensity distribution (red–white) and the maximum intensity projection on each dimension (gray–white) are shown. Volume size: 10 μm × 10 μm × 20 μm. The wavefront aberration is shown at the upper right. (d), (e) TPM imaging stacks of the dendrite model with distorted 3D PSF in (b) and (c), separately. Volume size: 50 μm × 50 μm × 20 μm. (f)–(h) Typical cross sections in (d). The z_0 plane is defined at the depth where the close double dendrites appear the most obviously. Scale bar: 10 μm. (i)–(k) Typical cross sections in (e). The z_0 plane is defined at the depth where the dendrites at z_f = 0 have the maximum intensity in the imaging stack. (l) The normalized intensities along solid lines in (f)–(h). (m) The normalized intensities along solid lines in (i)–(k). In (l) and (m), intensity normalization is performed with a reference of the maximum value of the three lines. (g), (h) and (i)–(k) have the same color bar, respectively.

We further simulate the 3D PSF and two-photon images of the dendrite model under the hybrid wavefront aberrations of astigmatism and coma, as shown in Fig. 4. We show the 3D PSF with the combination of these two Zernike modes, in which the distorted PSF contains two main lobes at different axial positions [Fig. 4(a)]. The same dendrite model is used as above. Three typical cross sections are shown in Figs. 4(b)–4(d). It can be seen that, with the distorted 3D PSF of two main lobes, the experimental phenomena can be reproduced well. The images at different depths vary as the axial distribution of 3D PSF is asymmetric. The artifact at the $z_0 - 3$ μm plane is barely seen, while at the z_0 plane it becomes obvious [Fig. 4(i)]. The shift of dendrite positions at different depths is attributed to the axial tilt of the 3D PSF. In addition, the relative orientations of PSF and samples also matter, as the final image is the 3D convolution between the PSF and samples. As the two main lobes of the 3D PSF [Fig. 4(a)] separate on the *x* axis but coincide on the *y* axis, when the sample is along the *x* axis, the artifact disappears [Fig. 4(j)]. It suggests that the simulation results agree well with all experimental observations.

Besides, we notice that such phenomena have rarely been reported in WFM. To show the difference of image artifacts induced by wavefront aberrations in TPM and conventional WFM, we simulate the PSF and dendrite images under the same aberration conditions as above. We set the emission wavelength of WFM at 520 nm and show the distorted emission PSF [Fig. 4(e)]. We also show three images at different cross sections [Figs. 4(f)–4(h)]. Due to the lack of optical sectioning capability in WFM, the fluorescence signals at other depths near the imaging plane will cause background signals to the imaging plane. Therefore, different from that in TPM, the image of a dendrite at $z_f = 5$ μm appears at the imaging focal plane of $z_f = 0$. Moreover, for the same aberration, there is a larger Zernike aberration coefficient because the emission wavelength is considered in WFM, which is shorter compared to the infrared excitation wavelength in TPM. Thus, the distortion of 3D PSF is more serious in WFM than in TPM. As shown in Figs. 4(f)–4(h), the dendritic image is broader due to the background signals, the PSF is distorted more severely in WFM, and no closely spaced double-dendritic artifacts are observed.

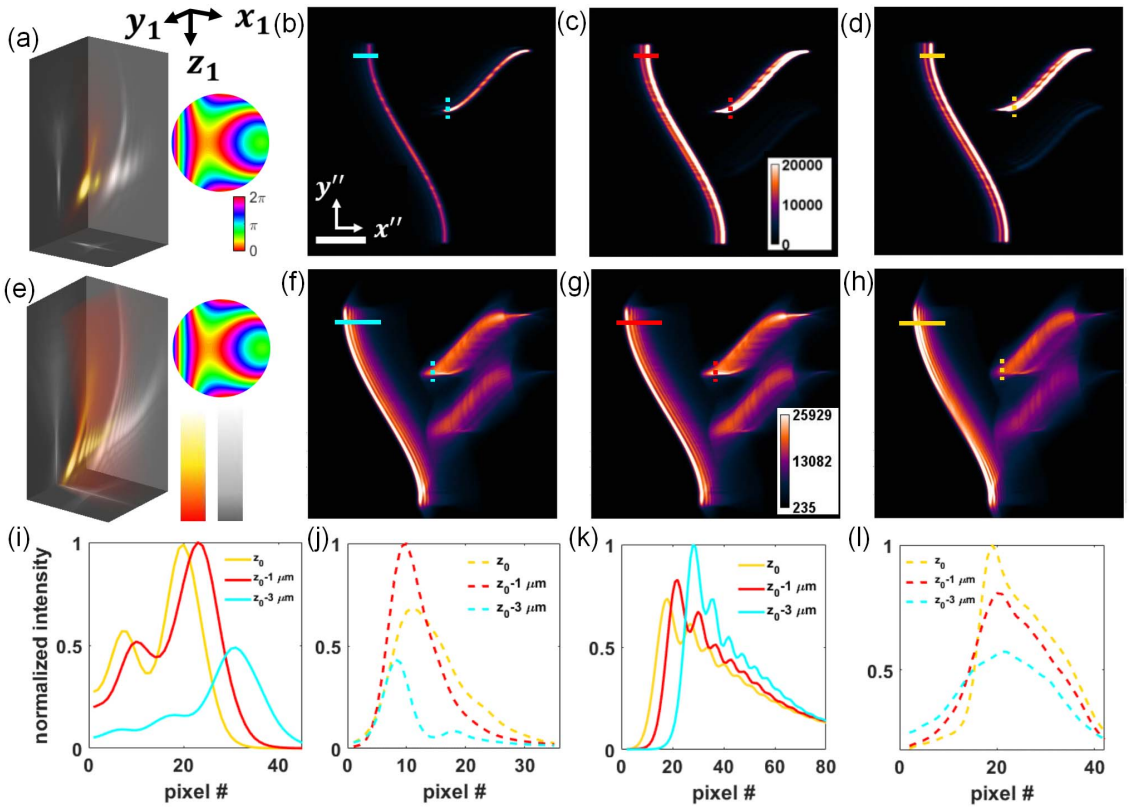

Fig. 4. Numerical simulation of distorted 3D PSF and the images of the dendrite models under the mixed wavefront aberrations in TPM and WFM. (a) Distorted 3D excitation PSF in TPM, with Zernike coefficients $W_2^2 = 0.3$ μm and $W_3^1 = 0.1$ μm. Both the 3D normalized intensity distribution (red–white) and the maximum intensity projection on each dimension (gray–white) are shown. Volume size: 10 μm × 10 μm × 20 μm. The mixed wavefront aberration is shown at the upper right. (b)–(d) Cross sections of the TPM imaging simulation of the dendrite model. The z_0 plane is defined at a depth in the stack where the close double dendrites appear the most obviously. Scale bar: 10 μm. (e) Distorted 3D emission PSF in WFM, with the same wavefront aberrations as that in TPM. (f)–(h) Cross sections of the WFM imaging simulation of the dendrite model. The z_0 plane is defined at a depth that has the best imaging contrast of the long dendrite. Scale bar: 10 μm. (i) The normalized intensities along solid lines in (b)–(d). (j) The normalized intensities along dotted lines in (b)–(d). (k) The normalized intensities along solid lines in (f)–(h). (l) The normalized intensities along dotted lines in (f)–(h). In (i)–(l), intensity normalization is performed with a reference of the maximum value of the three lines. (b)–(d) and (f)–(h) have the same color bar, respectively.

4. Discussion

In this paper, we report the local artifacts of divided parallel structures at certain depths in two-photon imaging of dendrites beneath blood vessels. Through numerical simulations, we find that the artifacts are mainly induced by astigmatism and coma, resulting from the cylindrical shape of the blood vasculature and sample tilting, respectively. Besides, we numerically verify that the artifacts in TPM and WFM are different.

It should also be noted that the artifacts reported here are so localized that the adoption of adaptive optics becomes less valuable. This is because the compensation wavefront is only constructive in a limited area, but destructive elsewhere. However, such artifacts should be recognized in properly interpreting the imaging results.

Acknowledgement

L.K. thanks Tsinghua University and Beijing Frontier Research Center for Biological Structure for the support. This study was supported by the National Natural Science Foundation of China (Nos. 61831014, 61771287, and 32021002), Tsinghua University Initiative Scientific Research Program (No. 20193080076), "Bio-Brain+X" Advanced Imaging Instrument Development Seed Grant, and Graduate Education Innovation Grants, Tsinghua University (No. 201905J003).

References

1. D. Wang and J. Xia, "Optics based biomedical imaging: principles and applications," J. Appl. Phys. **125**, 191101 (2019).
2. K. Akassoglou, M. Merlini, V. A. Rafalski, R. Real, L. Liang, Y. Jin, S. E. Dougherty, V. D. Paola, D. J. Linden, T. Misgeld, and B. Zheng, "*In vivo* imaging of CNS injury and disease," J. Neurosci. **37**, 10808 (2017).
3. Y. Ozeki, "Molecular vibrational imaging by stimulated Raman scattering microscopy: principles and applications," Chin. Opt. Lett. **18**, 121702 (2020).
4. L. Zhu, Y. Wang, Y. Yuan, H. Zhou, Y. Zhao, and Z. Ma, "Spectral domain optical coherence tomography with sub-micrometer sensitivity for measurement of central corneal thickness," Chin. Opt. Lett. **17**, 041701 (2019).
5. G. Sancataldo, L. Silvestri, A. L. A. Mascaro, L. Sacconi, and F. S. Pavone, "Advanced fluorescence microscopy for *in vivo* imaging of neuronal activity," Optica **6**, 758 (2019).

6. B. A. Wilt, L. D. Burns, E. T. Wei Ho, K. K. Ghosh, E. A. Mukamel, and M. J. Schnitzer, "Advances in light microscopy for neuroscience," Annu. Rev. Neurosci. **32**, 435 (2009).
7. I. Y. Koh, W. B. Lindquist, K. Zito, E. A. Nimchinsky, and K. Svoboda, "An image analysis algorithm for dendritic spines," Neural. Comput. **14**, 1283 (2002).
8. M. U. Ghani, F. Mesadi, S. D. Kanık, A. O. Argunsah, A. F. Hobbiss, I. Israely, D. Unay, T. Tasdizen, and M. Cetin, "Dendritic spine classification using shape and appearance features based on two-photon microscopy," J. Neurosci. Methods **279**, 13 (2017).
9. M. Li, F. Liu, H. Jiang, T. S. Lee, and S. Tang, "Long-term two-photon imaging in awake macaque monkey," Neuron **93**, 1049 (2017).
10. Z. Gu, X. Wang, J. Wang, F. Fan, and S. Chang, "Sidelobe suppression and axial resolution enhancement in 4pi microscopy with higher-order radially polarized Laguerre–Gaussian beams using subtractive imaging," Chin. Opt. Lett. **17**, 121103 (2019).
11. J. Zeng, P. Mahou, M.-C. Schanne-Klein, E. Beaurepaire, and D. Débarre, "3D resolved mapping of optical aberrations in thick tissues," Biomed. Opt. Express **3**, 1898 (2012).
12. M. J. Booth, "Adaptive optics in microscopy," Philos. Trans. A Math. Phys. Eng. Sci. **365**, 2829 (2007).
13. F. Helmchen and W. Denk, "Deep tissue two-photon microscopy," Nat. Methods **2**, 932 (2005).
14. W. Denk, J. H. Strickler, and W. W. Webb, "Two-photon laser scanning fluorescence microscopy," Science **248**, 73 (1990).
15. K. Svoboda and R. Yasuda, "Principles of two-photon excitation microscopy and its applications to neuroscience," Neuron **50**, 823 (2006).
16. C. Jin, L. Kong, H. Dana, H. Xie, L. Cao, G. Jin, and Q. Dai, "Advances in point spread function engineering for functional imaging of neural circuits *in vivo*," J. Phys. D **53**, 383001 (2020).
17. Y. Liu, P. Lai, C. Ma, X. Xu, A. A. Grabar, and L. V. Wang, "Optical focusing deep inside dynamic scattering media with near-infrared time-reversed ultrasonically encoded (TRUE) light," Nat. Commun. **6**, 5904 (2015).
18. R. Horstmeyer, H. Ruan, and C. Yang, "Guidestar-assisted wavefront-shaping methods for focusing light into biological tissue," Nat. Photon. **9**, 563 (2015).
19. N. Ji, "Adaptive optical fluorescence microscopy," Nat. Methods **14**, 374 (2017).
20. L. Kong and M. Cui, "*In vivo* deep tissue imaging via iterative multiphoton adaptive compensation technique," IEEE J. Sel. Top. Quantum Electron. **22**, 40 (2016).
21. J.-H. Park, W. Sun, and M. Cui, "High-resolution *in vivo* imaging of mouse brain through the intact skull," Proc. Natl. Acad. Sci. U.S.A. **112**, 9236 (2015).
22. J.-H. Park, L. Kong, Y. Zhou, and M. Cui, "Large-field-of-view imaging by multi-pupil adaptive optics," Nat. Methods **14**, 581 (2017).
23. P. T. So, C. Y. Dong, B. R. Masters, and K. M. Berland, "Two-photon excitation fluorescence microscopy," Annu. Rev. Biomed. Eng. **2**, 399 (2000).
24. B. Richards and E. Wolf, "Electromagnetic diffraction in optical systems. II. Structure of the image field in an aplanatic system," Proc. Roy. Soc. A **253**, 358 (1959).
25. Q. Li, "Optimization of point spread function of a high numerical aperture objective lens: application to high resolution optical imaging and fabrication," PhD Thesis (Ecole Normale Supérieure de Cachan, 2014).
26. M. Born and E. Wolf, *Principles of Optics: Electromagnetic Theory of Propagation, Interference and Diffraction of Light* (Cambridge University, 1999).
27. M. A. Neil, M. J. Booth, and T. Wilson, "New modal wave-front sensor: a theoretical analysis," J. Opt. Soc. Am. A **17**, 1098 (2000).
28. S. L. Jacques, "Optical properties of biological tissues: a review," Phys. Med. Biol. **58**, R37 (2013).
29. B. Huang, W. Wang, M. Bates, and X. Zhuang, "Three-dimensional super-resolution imaging by stochastic optical reconstruction microscopy," Science **319**, 810 (2008).
30. M. Tobias, B. A. Gutwein, and A. Rohrbach, "Light-sheet microscopy in a glass capillary: feedback holographic control for illumination beam correction," Opt. Lett. **42**, 350 (2017).
31. R. Turcotte, Y. Liang, and N. Ji, "Adaptive optical versus spherical aberration corrections for *in vivo* brain imaging," Biomed. Opt. Express **8**, 3891 (2017).